Influence of microstructural features and deformation-induced martensite on hardening of stainless steel by cryogenic ultrasonic impact treatment

M.A. Vasylyev[a], B.N. Mordyuk[a,*], S.I. Sidorenko[b], S.M. Voloshko[b], A.P. Burmak[b]

[a] Department of Physical Fundamentals of Surface Engineering, Kurdyumov Institute for Metal Physics, NAS of Ukraine, 36 Academician Vernadsky Blvd., UA-03142 Kyiv, Ukraine
[b] Metal Physics Department, Igor Sikorsky National Technical University of Ukraine, 37 Peremohy ave., UA-03056 Kyiv, Ukraine

ARTICLE INFO

ABSTRACT

Ultrasonic impact treatment of stainless steel AISI 321 was carried out at room temperature (in the argon environment – argon-UIT) and at cryogenic temperature (in liquid nitrogen – cryo-UIT) in the constrained conditions with application of the same mechanical energy to the treated specimens. The time dependencies of the surface hardness HV after the cryo-UIT and argon-UIT processes were of sigmoidal and parabolic shapes, respectively. The microstructural evolution of the surface layers of the deformed specimens was studied by X-ray diffraction (XRD), optical microscopy (OM), transmission electron microscopy (TEM) and selective area electron diffraction (SAED) analyses. The volume fractions of the deformation-induced α' ($V_{\alpha'}$) and ε (V_ε) martensites were estimated using XRD approach and by magnetic and density measurements. Compared to the room temperature UIT in the argon environment (argon-UIT), the liquid nitrogen UIT generates a higher density of the deformation twins and stacking faults. In addition, a higher $V_{\alpha'}$ ($\sim 53\%$) and V_ε ($\sim 3.5\%$) were observed after cryo-UIT in deeper surface layers ($\sim 200\ \mu m$). The argon-UIT process leads to the formation of either rectangular twin blocks or dislocation cells, which size ranged 200–500 nm. Conversely, after cryo-UIT ($\bar{e} \approx 0.95$), a nanoscale grain structure of heterogeneous nature (α' and γ phases) was formed in the outmost surface layer simultaneously with the areas filled with networks of deformation twins and stacking faults. The minimum grain size of α'-martensite $D_{\alpha'}$ and austenite D_γ was respectively 25 and 45 nm, and twin thickness/spacing was of 60–120 nm. Both types of the microstructure contribute to the material strength and result in higher hardness of the cryo-UIT processed specimens (~ 5–5.66 GPa) compared to that of the argon-UIT processed ones (~ 4.3 GPa). With the increase in Zener-Hollomon parameter $\ln Z$, the grain/twin/spacing size is decreased while the $V_{\alpha'}$ and surface microhardness HV are increased.

1. Introduction

Austenitic steels are widely used in industry due to its high resistance to corrosion, oxidation and high strength over a wide temperature range. These properties allow using these steels in biomedicine, chemical industry, and in the transportation facilities for liquefied natural gas, operating at cryogenic temperatures.

Accounting for the determinative role of the surface in the operational properties of materials and lifetime of constructions, one of the most important and widely studied areas is the mechanical modification of metallic surfaces using the methods of the surface severe plastic deformation (S²PD). A lot of studies during the last decades demonstrate the beneficial effects of the surface nanostructurization on the anticorrosion property, wear resistance and fatigue durability of metallic materials. Several S²PD methods, such as shot peening [1],

surface mechanical attrition treatment (SMAT) [2–4], surface grinding [5], and ultrasonic impact treatment (UIT) [6–8] applied to stainless steels allow generating nanoscale grain structures in their surface layers, and significantly increase their physical and mechanical properties.

It is shown that among the factors leading to the mechanical nanostructuring, such as a high strain extent and high strain rate, the processing temperature is also an important parameter, which exerts a significant influence on the deformation mechanisms [9–12]. Thus, the temperature rise facilitating dynamic recrystallization (DRX) may limit the minimum grain size of the formed microstructure [13,14]. Additionally, the deformation heating can initiate phase transformations and facilitate further structural refinement through the strain induced heterogeneity of the phase composition in the surface layer. Conversely, the negative or cryogenic [12,15–18] temperatures applied at the SPD

(S^{2}PD) processes can essentially slow down the DRX or even almost completely hindered it. The outcome is the formation of ultrafine and/or nanoscale grain structures even in the materials of relatively low melting temperature (high DRX ability), such as copper [11,12], aluminium [19] and magnesium [20] alloys.

Cryogenic deformation of the stainless steels, particularly cryogenic tension [17,21–23], compression [24] or rolling [25], was shown to induce higher quantities of deformation twins, shear bands and stacking faults than those observed at room temperature. Strain induced epsilon- and alpha′-martensites were also formed more easily. The peculiarities of the strain induced structure and phase transformations in stainless steels at multiple impact loads were mainly analyzed in the ambient air (SMAT [2,3] or in the vacuum (UIT [6,7]). Only a few works were addressed to the outcomes of cryogenic SMAT [26] or cryogenic laser shock processing [27,28]. At the same time, the variation of the processing intensity and environmental/temperature conditions can be useful in the obtaining of new materials comprised both the microstructural and phase heterogeneities, which may provide the gradient mechanical and magnetic properties [29].

This work aims to study the microstructural features and phase transformations in stainless steel AISI 321 induced by the argon-UIT and cryogenic-UIT processes. The operative hardening mechanisms and the influence of Zener-Hollomon parameter were also addressed.

2. Experimental details

An austenitic stainless steel AISI-321, which chemical composition is given in Table 1, was used in this study. Disk specimens (thickness $h = 2$ mm and diameter $d = 6$ mm) of this steel were initially annealed for 1 h at 750 °C; the resulting initial average grain size was 50–100 μm. These specimens were exposed to UIT at different processing temperatures.

Details of the UIT process can be found elsewhere [6–8,30–33]. In this study, ultrasonic equipment schematically shown in Fig. 1 contained an ultrasonic generator with a frequency of 21.6 kHz and a power output of 0.6 kW. The cylindrical pin positioned between the tip of an ultrasonic horn and the specimen produced repetitive impacts by the treated surface. Impacts frequency induced by vibration of the ultrasonic horn was of ~1–2 kHz. The specimen was placed into a socket made in the hardened steel holder and underwent the quasi-hydrostatic shock compression during each impact. The estimated strain rate ranges 0.1–1.5 s^{-1} and decrease far from the treated surface. The UIT process lasted from 50 to 250 s and induced severe plastic deformation of the specimen surface and near the surface area. Two series of similar specimens were processed: the first one in the argon environment (argon-UIT) and the second one in liquid nitrogen (cryo-UIT). A special sealed chamber [31,33,34] filled with gaseous argon or liquid nitrogen was used (Fig. 1).

During each impact, the treated specimen was restricted in every direction except for a minor outflow of the surface layer which occurs around the outer edge of the treated disk specimen, i.e. the deformation occurs in so-called quasi-isostatic conditions (Fig. 1b). To estimate the effective strain $\bar{e}$, the following expression was used [30,35]:

$$\bar{e} = (\sqrt{2}/3)[(\varepsilon_1-\varepsilon_2)^2 + (\varepsilon_2-\varepsilon_3)^2 + (\varepsilon_3-\varepsilon_1)^2]^{1/2} \tag{1}$$

where $\varepsilon_1 = (h_0 - h_P)/h_0$, $\varepsilon_2 = \varepsilon_3 = (d_0 - 2p)/d_0$ are the principal strains, h_0 and h_P are thicknesses of the initial and as-treated disk-samples measured on their axis, d_0 is an initial diameter of the disk-sample, and p is a height of the pileup formed around the outer edge of

Table 1
Chemical composition of the stainless steel AISI-321 (wt%, balance is Fe).

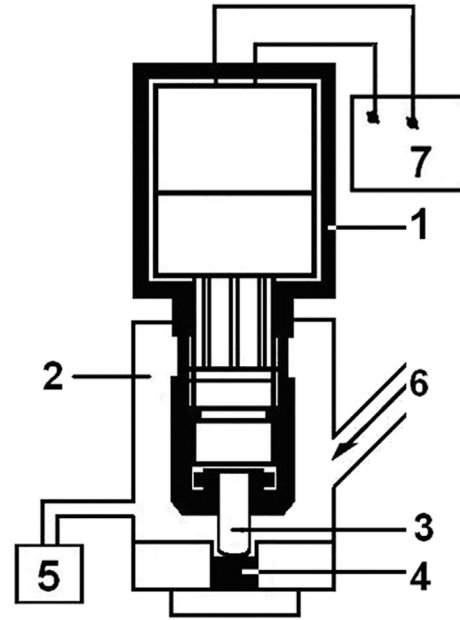| C	Si	Mn	Cr	Ni	Ti	P	S
≤ 0.07	≤ 0.8	1–2	17–19	9–11	0.7	< 0.03	< 0.02

Fig. 1. Scheme of the specimen loading unit at the UIT process: 1 is the ultrasonic transducer with a step-like horn; 2 is a hermetic chamber; 3 is a pin; 4 is a disc-specimen; 5 is manometer; 6 is a channel used for filling of the chamber with gas or liquid nitrogen; 7 is an ultrasonic generator.

the treated disk-sample after the UIT processing for a certain time.

Microhardness HV of the surfaces and cross-sections were respectively measured at loads of 100 and 20 g and a dwell time of 10 s using a PMT-3M microdurometer.

Since the UIT process was performed at different temperatures in this study, the Zener-Hollomon parameter representing the combined effect of strain rates ($\dot{\varepsilon}$) and deformation temperatures (T) was calculated using the well-known expression [11,12]:

$$\ln Z = \ln \dot{\varepsilon} + \ln(Q/RT). \tag{2}$$

Using the activation energy for deformation of this stainless steel $Q \approx 33.4$ kJ/mol adopted after [36] the ln$Z$ estimations were performed for experimental conditions used both in this study and in the literature (see Table 2). The actual sample temperature (T) is normally larger than the nominal deformation temperature due to the transient temperature rise ΔT induced by plastic deformation, which can be accounted for as follows [11,30]:

$$\Delta T = (\beta/C_V m\rho) \int_{\bar{e}_1}^{\bar{e}_2} \sigma_Y \bar{e}\, \mathrm{d}\bar{e}, \tag{3}$$

where $\beta \approx 0.9$–0.95 is a factor for conversion of the deformation work done into heat, ρ is the density, C_V is the specific heat capacity, σ_Y is the yield stress that correlates to the Vickers hardness through the Tabor's relation $\sigma_Y \approx 0.3HV$, $\bar{e}$ is the effective strain. This expression is valid in our case owing to the adiabatic character of the UIT process (high strain rate and very short deformation duration during each impact).

Microstructural analysis of the surface layers was performed using optical microscopy (OM), X-ray diffraction (XRD) analysis, transmission electron microscopy (TEM) and selective area electron diffraction (SAED) studies.

Optical metallography of the cross-sections of the original and treated specimens was carried out using a Neophot-32 microscope. The grain boundaries were etched using a NITAL reagent.

TEM observations and SAED studies were carried out using a JEM 100 CX-II microscope. The plane-view TEM foils were prepared from different sections of treated specimens (the top surface layer and ~30 μm from the outer surface). They were mechanically polished on the untreated side of the sample followed by electro-polishing by means of a twin-jet technique. One-side polishing was used to obtain the foil

Table 2
Parameters of stainless steels after various treatments.

Sample	Treatment	$\bar{e}$	$\dot{\varepsilon}$, s⁻¹	T_N, K	ΔT, K	$\langle \ln Z \rangle$	$V_{\alpha'}$, % (X/M)[a]	Λ_{tw}, nm	$D_\gamma/D_{\alpha'}$, nm	HV, MPa	Refs.
AISI 321	Vacuum-UIT-2	0.45	10³	293	0–40	20	12/6	–	29/22ᵗ	3.2–4.7ᵗ	[7]
	Vacuum-UIT-4	0.81	10³				23/12	40–200	26/15ᵗ	3.5–4.5ᵗ	
	Argon-UIT-1	0.24	10³	293	80–150	17	20/5	~100	32/27ᵗ	3.5ᵗ	Present study
	Argon-UIT-2.5	0.7	10³				23/18	200–500	43/36ᵗ	4.6ᵗ	
	Cryo-UIT-1	0.24	10³	77	100–180	26	14/20	–	38/8ᵗ	4.4ᵗ	
	Cryo-UIT-3.5	0.95	10³				54/37	60–120	46/24ᵗ	5.3–5.8ᵗ	
AISI 321 (1Cr18Ni9Ti)	RT-C	0.91	10⁻³	293	0–40	6	14.2/–	250–650	20–120	–	[24]
	Cryo-C	0.91	10⁻³	77	30–80	24	43.4/–	60–74	40–100	–	
AISI 316	RT-MDF	0.4	10⁻³	293	0–80	5	–/5		–/500	3.2	[18]
		2.4	10⁻³				–/10	~30	63/63	3.8	
	Cryo-MDF	0.4	10⁻³	77	40–100	22	–/33	10–300	–	4.2	
		2.4	10⁻³				–/74	~20	–/45	4.6	
AISI 304	RT-LSP	–	10³	293	0–40	20	0/–	300–500	80–150ᵗ	2.6ᵗ	[27]
	Cryo-LSP	–	10³	77	0–40	50	35.3/–	50–200	30–100ᵗ	3.2ᵗ	
AISI 304	RT-SMAT-L	0.07	10³	293	40–80	18	95/–ᵗ	–	–/10ᵗ	5.0ᵗ	[3]
							70/–ᵈ	–	200/60ᵈ	4.0ᵈ	
	RT-SMAT-H	0.2	10⁵	293	40–80	23	23/–ᵗ	–ᵗ	250/120ᵗ	5.0ᵗ	
							14/–ᵈ	20–50ᵈ	–/200ᵈ	4.4ᵈ	

$\bar{e}$ is effective (true) strain, $\dot{\varepsilon}$ is the strain rate, T_N is nominal temperature, ΔT is transient temperature rise, $\langle \ln Z \rangle$ is an average Zener-Hollomon parameter, $V_{\alpha'}$ is the volume fraction of α' martensite, Λ_{tw}, is the twin/shear band spacing, D_γ and $D_{\alpha'}$ are the crystallite size for austenite and martensite, HV is the Vickers hardness, ᵗ and ᵈ indicate the data obtained from the top and deeper layers, respectively. UIT is ultrasonic impact treatment; C is compression; SMAT-L and SMAT-H are low and high energy surface mechanical attrition treatments; MDF is multidirectional forging; LSP is laser shot peening.

 [a] X and M respectively denote X-ray and magnetic methods for $V_{\alpha'}$ assessment.

from the outmost surface layer.

The XRD investigations were carried out using a Rigaku Ultima-IV diffractometer (Cu-$K\alpha$ irradiation). Assuming that the analyzed microstructure of the surface layer of 10–20 mkm thick was sufficiently homogeneous a Pseudo-Voigt fitting function incorporating both the Gaussian and Lorentz function) was used for fitting XRD peaks. While using the Scherrer equation, one should be aware of possible large error (~30%) of the assessed grain size when neglecting the strain broadening, especially in the case of low amounts of alpha-martensite [37]. Thus these data can be reliably analyzed only in a combination with TEM observations. Based on the measured width and estimated physical broadening B of diffraction peaks, the contributions of the size D of coherent areas and the mean lattice micro-strain η were estimated accounting for the appropriate diffraction angle θ [7]:

$$B \cos \theta = (0.9\lambda/D) + \eta \sin \theta. \qquad (4)$$

Estimations of dislocation densities in the original and deformed specimens were carried out using the magnitudes of D, η and Burgers vectors b for appropriate phases [38]:

$$\rho = 2\sqrt{3}\eta/Db. \qquad (5)$$

Volume fractions of strain-induced ε (V_e) and α' ($V_{\alpha'}$) martensite were assessed by means of the formula [7,17,22]:

$$V_i = \frac{1}{n_i} \sum_{j=1}^{n_i} \frac{I_i^j}{R_i^j} \Bigg/ \left(\frac{1}{n_\gamma} \sum_{j=1}^{n_\gamma} \frac{I_\gamma^j}{R_\gamma^j} + \frac{1}{n_\alpha} \sum_{j=1}^{n_\alpha} \frac{I_{\alpha'}^j}{R_{\alpha'}^j} + \frac{1}{n_\varepsilon} \sum_{j=1}^{n_\varepsilon} \frac{I_\varepsilon^j}{R_\varepsilon^j} \right), \qquad (6)$$

which accounts for the number of peaks (n) of the phase i used in calculations, the integrated intensity (I) of the reflecting plane, and the material scattering factor (R). The following diffraction lines were used: {002} and {101} reflections for ε-martensite, {110} and {200} reflections for α'-martensite and {111} and {200} reflections for γ-austenite. The present measurements are expected to be independent of texture effects. Besides, one should account for the worsening of the accuracy of the method when the volume fraction of the analyzed phase becomes lower than about 4%.

Taking different crystal structures and densities of the austenite and α'-martensite phases into account, the content of α'-martensite phase was also determined by measuring the density of the specimens after the UIT process and comparing it to their initial densities. The α'-martensite content is assumed to be a linear function of the density,

despite some error possibly occurred owing to the crystal defects in both phases.

The densities of the austenite and α'-martensite phases were determined based on the previous X-ray diffraction (XRD) analysis using the equation [39]:

$$\rho = nA/VN_A \qquad (7)$$

where n is the number of atoms in a unit cell (two in α'-martensite, four in austenite), A is the atomic weight, V is the volume of a unit cell and N_A is Avogadro's number. The volume of the unit cell was assessed using the XRD data. Average atomic weights were calculated from the chemical composition of the steel (Table 1). The density was measured by means of the Archimedean principle. The mass of the samples was measured with a RADWAG XAS 100/C balance (accuracy of 0.0001 g). The measurements were performed both in the ambient air and by immersing the specimens in a distilled water contained a wetting agent. In the latter case, the specimen was supported with 0.1 mm thin fishing line, and the volume of the specimen was determined. Thus, the density of the specimen was calculated by using equation related the mass of the specimen weighed in air m_A and in distilled water m_W and the density of distilled water ρ_W:

$$\rho = m_A \rho_W / m_W. \qquad (8)$$

The measurements were performed at room temperature, which assumed to be constant owing to its negligible variations (≤1 °C) during the measurements. All samples were measured three times to improve the accuracy of the assessed contents of α'-martensite. Accounting for the accuracy of the used balance and the mass of the studied specimens the $V_{\alpha'}$ assessment accuracy was adopted to be ± 1%.

Assuming the α'-martensite is the only ferromagnetic phase and considering the sample mass, the volume fraction of α'-martensite was also determined by the following expression [6,35]:

$$V_\alpha = M_s/M_s^0, \qquad (9)$$

where M_S^0 is the saturation magnetization of α'-martensite, $M_S^0 \approx 146$ Am² kg⁻¹. Saturated magnetization M_S of as-treated specimens was measured using ballistic magnetometer at room temperature in a saturated magnetic field of ~4·10³ kAm⁻¹. In this case, a relative experimental error of the $V_{\alpha'}$ assessment caused by the specimen size was < 1%.
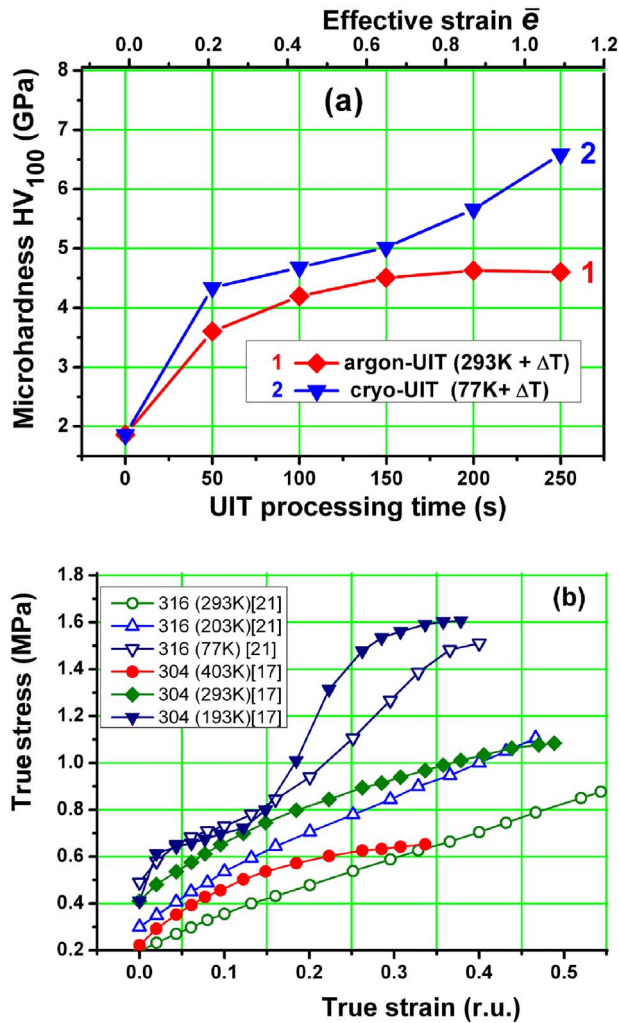
Fig. 2. Dependencies of microhardness *HV* of the argon-UIT (1) and cryo-UIT (2) processed specimens of AISI 321 steel on the processing time *t* and effective strain $\bar{e}$ assessed using Eq. (1)(a) and the 'true stress – true strain' tensile curves registered for AISI 304 [17] and AISI 316 [21] at different test temperatures (b).

3. Results and discussion

3.1. Hardness evolution

Fig. 2a compares the hardness evolutions observed for the samples underwent argon-UIT and cryo-UIT at the same process intensities. It can be seen that after cryo-UIT, the *HV* magnitudes are always higher than those registered after the argon-UIT process. Additionally, work hardening rates are different in the studied cases. After rapid hardening on the first stage of straining (at small processing time up to 50 s) the hardening decreases to reach saturation. For the cryo-UIT process (curve 2 in Fig. 2a), three distinct hardening stages are noticed; initial high hardening rate supported by dislocation activity and twinning in austenite changes with the hardening deceleration/plateau owing to intensive formation of epsilon martensite at approx. e ≈ 0.1–0.15, and then (at approx. e ≈ 0.2–0.3) it increases again when the increasing volume fraction of alpha phase is formed at the expense of epsilon phase. Actually, the shape of the latter dependence becomes of sigmoidal shape. Both the *HV* increase and the change of the shape of the 'hardness-strain' dependence at the cryo-UIT process are naturally affected by the microstructural features, which are dependent on the straining temperature.

Such hardness behavior after UIT is in good correlation with the deformation behavior reported for the stainless steels AISI 304 [17,22]

and AISI 316 [21], which tensile 'stress-strain' ('σ–ε') curves are shown in Fig. 2b for the sake of comparison. While the room temperature 'σ–ε' curves are of parabolic shape, a sigmoidal shape of the 'σ–ε' curves is registered for straining at negative or cryogenic temperatures. Following a number of reports regarding the reasons of different hardening behaviors of austenitic steels strained at room or cryogenic temperatures [2,7,17,21–23], the $\gamma \to \varepsilon$ and $\gamma \to \alpha'$ martensitic transformations can be concluded to play crucial roles in the strain hardening of these steels. A liquid nitrogen temperature promotes easier twinning and martensitic transformations that intensify the grain refinement process at the later stages of straining owing to the multi-phase nature of the microstructure formed. The fine-grained microstructure is another well-documented factor of hardening, which should be considered. It is usually formed by multiple impact loading [1–4,6–8], at cryogenic laser shot peening [27,28] or cryogenic compression [24]. This factor is expected to be involved in the latter stages of the UIT process, and a number of experimental findings confirming this expectation are described below.

Correlation of *HV* profiles and microstructure in the surface layers is visible in Fig. 3, which shows the optical microscopy observations of the cross-sections of the specimens underwent UIT processes for 150 s. In comparison with the clear austenitic grains observed in the initial specimen (Fig. 3a), numerous twins and martensitic needles appear after deformation. Different martensite morphologies can also be recognized; both the parallel ε-martensite plates and more irregular α'-martensite are visible.

Despite the relatively uniform distribution of the martensite/twins in the specimens after both processes, comparing to the argon-UIT (Fig. 3b), the cryo-UIT process results in a finer grain structure in the surface layer (Fig. 3c).

The *HV* profiles in the cross-sections of the UIT processed specimens are shown in Fig. 3d. The *HV* increase is usually attributed to several factors including high density of dislocations, strain-induced martensitic phases, twins/stacking faults, and fine grains in the treated surface layers. The afore-mentioned factors are operative at different depths from the outmost surface underwent UIT processing. Thus, the different thickness of the hardened layers was obtained after different processing time and at various straining temperatures despite the same UIT intensities used. Below a certain depth, some of the hardening mechanisms exhaust (for instance, a Hall-Petch grain boundary factor operative mainly in the topmost surface layer), but the *HV* magnitudes are still higher than that of the original specimen. Therefore, the *HV* curves gradually decrease down to the initial *HV* magnitude.

The *HV* profiles observed after cryo-UIT lie above those registered for the argon-UIT processed specimens. Additionally, the thickness δh of the hardened layers was naturally increased with ongoing deformation. In comparison with the microhardness *HV* of the original specimen (~ 2.5 GPa), the *HV* magnitudes measured at a low load (20 g) reach ~ 6 and ~ 8.5 GPa on the argon-UIT and cryo-UIT processed surfaces, respectively. Accounting for the surface *HV* (Fig. 2a), these *HV* magnitudes seem to be slightly overestimated owing to some elastic strain occurred in the hardened surface beneath the indenter. The high volume fraction of ε and α' martensite, as well as nanotwins, can serve as an elastic reinforcing phase in the austenite 'matrix' [27], which might hinder the penetration of the indenter.

3.2. Results of XRD analysis

3.2.1. Phase composition

Fig. 4 shows the θ–2θ XRD patterns registered at room temperature for the original specimen and the specimens UIT-processed for 150 s. It is seen that the diffraction pattern of the argon-UIT processed specimen contains the diffraction peaks from the fcc-austenite (γ) and bcc-martensite (α'). At longer UIT times, a greater accumulated strain extent results in higher $V_{\alpha'}$ and thus higher peaks of the α'-martensite phase. This is consistent with the outcomes of the shock deformation [39], the
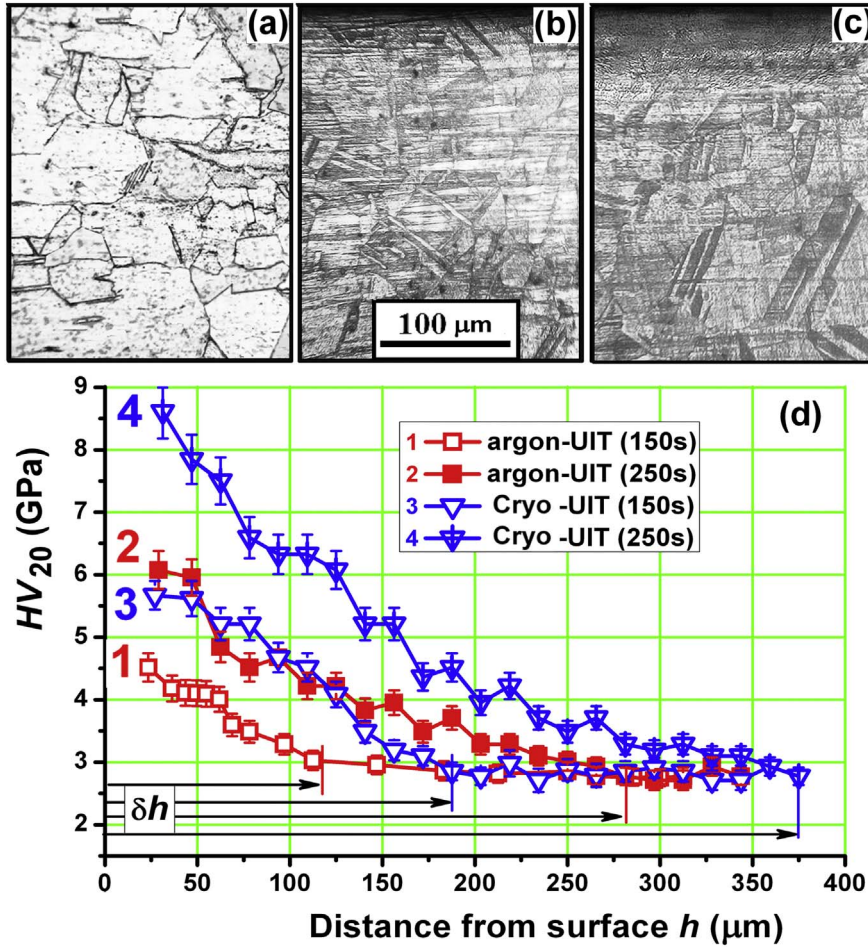
Fig. 3. OM observations of the microstructure (a–c) and microhardness *HV* profiles (d) of the cross-sections of the initial (a), argon-UIT (b, 1, 2) and cryo-UIT (c, 3, 4) processed specimens of AISI 321 austenitic stainless steel.

high energy shot peening [40], laser shot peening [27] or vacuum-UIT [6,7], where the $V_{\alpha'}$ was reported to increase as the processing time (strain extent) increase.

No evidence of the presence of ε-martensite was found from the XRD pattern registered after the argon-UIT process. Conversely, three phases were clearly observed in the diffraction pattern of the cryo-UIT processed specimen. This suggests that the microstructure of the surface layer of this specimen consists of the austenite and two strain-induced martensitic (ε and α′) phases (Fig. 4b). It is of interest that the ε-martensite did not disappear at relatively large strain extent ($\bar{e} \approx 0.7$) accumulated on the top surface of the specimen after the cryo-UIT process

lasted for 150 s. The ε-martensite formation is known to be less influenced by the strain variations since it is stress-assisted [22]. In our case, the constrained deformation in the course of the UIT-process provides high enough operative stresses in the processed specimen to facilitate $\gamma \rightarrow \varepsilon$ transformation. Although a number of studies report that ε-martensite usually disappeared after $\bar{e} \approx 0.3$ of tensile straining [17,21–23], after impact loading [40], high-energy shot peening [41], laser shot peening [27] or after vacuum UIT [7] carried out in the step-like mode avoiding the deformation heating of the treated specimen.

The estimations of the volume fraction $V_{\alpha'}$ of α′-martensite carried out using XRD analysis is compared to those obtained by
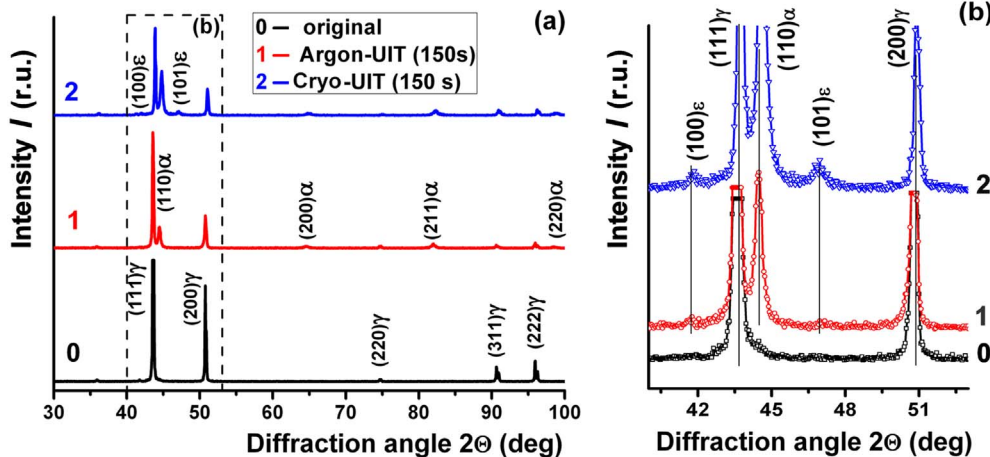

Fig. 4. XRD patterns (a) and magnified fragments of them (b) for the initial specimen (spectrum 0) and specimens processed by argon-UIT (spectrum 1) and cryo-UIT (spectrum 2) for 150s.
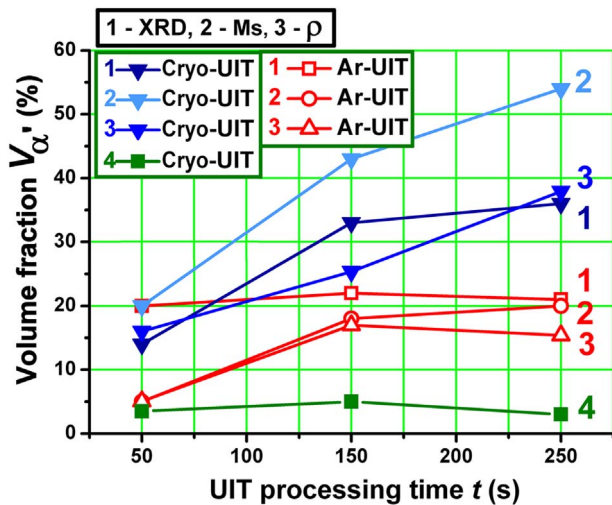
Fig. 5. Dependencies of the volume fraction $V_{\alpha'}$ (1–3) and V_ε (4) of the α′- and ε-martensite on the UIT process time evaluated using XRD analysis (1,4), and saturation magnetization (2) and density (3) measurements. Open and solid symbols respectively relate to argon-UIT and cryo-UIT processes.

magnetization/density measurements (Fig. 5). The α′-martensite contents $V_{\alpha'}$ measured with X-ray diffraction are shown as the functions on the UIT process time in Fig. 5 (curves 1). This $V_{\alpha'}$ assessed using Eq. (6) based on the intensity of appropriate peaks on the diffraction patterns (Fig. 4a) naturally, contains the data collected from the thin surface layer (for Cu Kα irradiation the thickness of the informative layer is about 10–20 μm dependently on the diffraction angle). Conversely, both the measurements of the saturation magnetization (curves 2 in Fig. 5) and density (curves 3 in Fig. 5) provide the information regarding the $V_{\alpha'}$ related to the bulk material. The $V_{\alpha'}$ curves registered by the magnetization/density measurements are higher in Fig. 5 indicating that the α′-martensite is formed in the bulk of the cryo-UIT-processed specimens. Moreover, the cryo-UIT induced $V_{\alpha'}$ is higher than that after argon-UIT, especially at the later stages of processing. Thus, a good correlation is seen between the increased $V_{\alpha'}$ and higher hardness and the thicker hardened layer formed after the cryo-UIT-process (Fig. 3d).

The XRD $V_{\alpha'}$ achieves ~20% after argon-UIT for 50 s, and further, it remains almost unchanged (till the argon-UIT time of 250 s). The measurements of saturation magnetization and density indicate a small $V_{\alpha'}$ after argon-UIT for 50 s, but with ongoing deformation at the argon-UIT process, the $V_{\alpha'}$ magnitudes become comparable to that obtained by XRD. Thus, an intensive formation of α′-martensite on the first stage of the argon-UIT process leading to rapid hardening (Fig. 2a) results in the initiation of γ → α′ transformation in the deeper layers, increasing an overall thickness of the hardened layer δh (curves 1, 2 with open symbols in Fig. 3d). Almost constant XRD magnitude of $V_{\alpha'}$ registered for the thin surface layer can be explained by the high probability of the reverse α′ → γ transformation, which can be facilitated by strain-induced temperature rise. Similar observations of the accelerated reverse α′ → γ transformation was reported for the stainless steel 304 either underwent SMAT followed by heating [42] or previously cold rolled and then shot peened at elevated temperatures [43]. In our case, highly constrained deformation facilitates adiabatic heating and strain-induced temperature rise (estimations using Eq. (3) gives ΔT ~ 80–180 K). Therefore, the reverse α′ → γ transformation is quite possible in a thin surface layer of the argon-UIT processed specimen examined by XRD.

The cryo-UIT process results in higher $V_{\alpha'}$ magnitudes, which were registered by all the methods used (curves 1–3 with solid symbols in Fig. 5). Magnetically evaluated $V_{\alpha'}$ achieves ~43 and 54% for 150 and 250 s, respectively. In this case, the XRD assessed $V_{\alpha'}$ magnitudes are lower than that evaluated magnetically and are comparable with those

obtained by density measurements. Despite a possible inaccuracy of the $V_{\alpha'}$ assessment methods used, this result can be considered as rather reliable since it correlates well to the literature data and thermodynamic analysis of the transformation probabilities at different temperatures [18,24,27].

It is well established that cryogenic deformation usually generates more strain-induced martensite than that at room temperature regardless the deformation scheme (Table 2) [18,24,27]. Normally, the spontaneous γ → α′ transformation would occur at temperature M_S when the free energy difference $\Delta G_{\gamma \to \alpha'}$ between the martensite phase and the austenite phase would be equal to the critical driving force ΔG_{crit}. At the higher temperatures ($T > M_S$) the critical driving force cannot be achieved due to low value of its chemical constituent ($\Delta G_{\gamma \to \alpha'}$), and some portion of additional mechanical driving force (ΔG_{mech}), which can be provided by plastic deformation, would be required to make the γ → α′ transformation possible. Actually, the difference between the $\Delta G_{\gamma \to \alpha'}$ and ΔG_{crit} increases rapidly with the temperature rise. Therefore, more mechanical energy is needed to trigger the deformation-induced martensite transformation at room temperature. A number of experimental [9,10,17,24,27] and theoretical [10,16] studies including thermodynamic modeling [44] have shown that the decrease in the straining temperature (down to cryogenic temperatures) results in higher α′-martensite owing to the significant decrease in the intrinsic stacking fault energy (SFE) of Fe–Ni–Cr alloys, which in its turn facilitates the easier formation of shear bands and twins. The results obtained in this study are in good correlation with the afore-mentioned literature.

The high volume fraction of α′-martensite is generally concluded to be one of the main hardening sources. However, there are some additional factors responsible for hardening. The estimations of the crystallite size, lattice microstrains and dislocation density (Fig. 6), which are addressed in the following subsection, confirm it.

3.2.2. Crystallite size and lattice microstrains

For two main phases (γ and α′), the contributions of the crystallite size D and the lattice micro-strains η were analyzed using Eq. (5) and the dependencies of the true physical broadening β on the diffraction angle θ, which were transformed in a linear function β = f(tan(θ)). The results of this analysis are shown in Fig. 6.

Refinement of coherent reflective areas D_γ of austenite (down to 30–40 nm) occurs already after UIT for 50 s in both the environment used. Thereafter, the D_γ slightly grows with ongoing deformation, especially at the argon-UIT process. The D_γ becomes about 40–60 nm after UIT for 250 s. The size of martensitic crystallites $D_{\alpha'}$ arise after UIT for 50 s is also in the nano-scale range, and it is slightly lower for the cryo-UIT ($D_{\alpha'} \approx$ 10–20 nm) than that for the argon-UIT ($D_{\alpha'} \approx$ 25–40 nm). The results for the argon-UIT seem to contradict to the TEM observations (Fig. 7d and Fig. 8c), which display the formation of the dislocation cell structure. However, one should account for the fact that the TEM foils were prepared from the sub-surface layer located at the depth of ~20–30 μm from the top surface that is larger than the penetration depth of the X-rays used (about 10 μm).

Lattice micro-strains η significantly affect the broadening of the diffraction profiles of α′ phase (curves 3, 4 in Fig. 6b). It is naturally related to high tetragonality of the α′ lattice owing to a high carbon content. The most marked lattice strains are observed for the argon-UIT processed specimen. Conversely, the lattice of austenite (γ) contains essentially lesser extents of micro-strain barely achieving 0.1% (curves 1, 2 in Fig. 6b).

Considering the estimated magnitudes of the size D of coherent reflective areas, lattice micro-strains η, and the dislocation densities ρ were also calculated to assess their evolutions in γ austenite and α′-martensite with ongoing deformation at the UIT process in different environments (Fig. 6c). It is seen that α′-martensite is characterized by higher ρ both after the argon-UIT and cryo-UIT processes (curves 3,4).
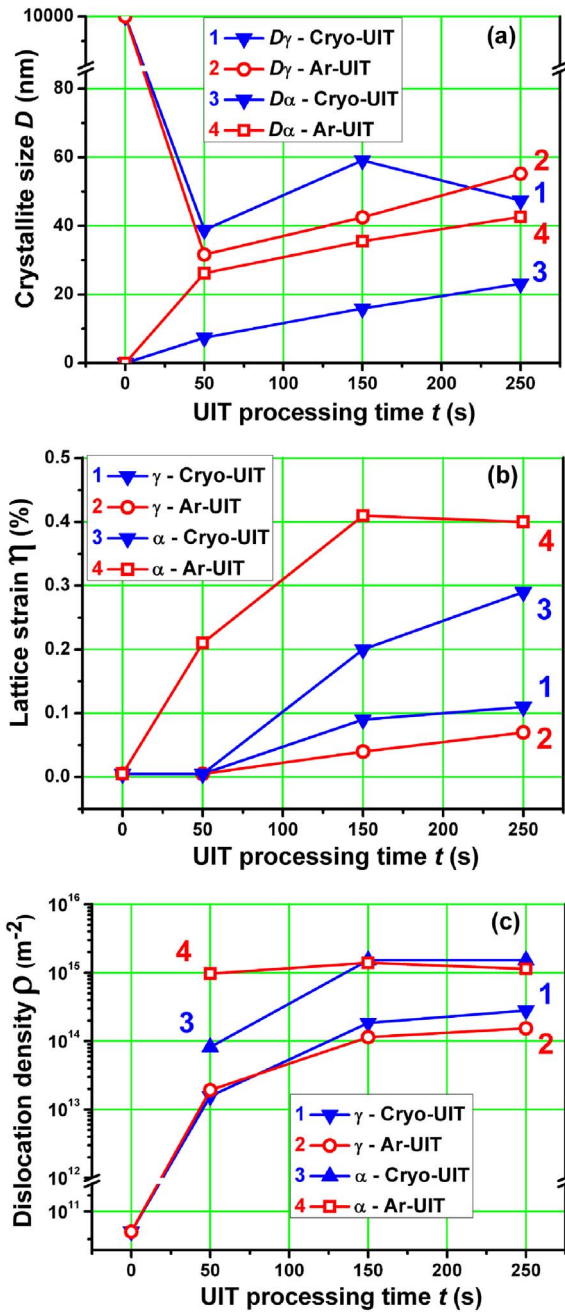
Fig. 6. Dependencies of the crystallite size D (a), lattice micro-strain η (b) and dislocation densities ρ (c) for γ (1, 2) and α' (3, 4) phases in the argon-UIT (open symbols) and cryo-UIT (solid symbols) processed specimens on the processing time evaluated using XRD analysis.

3.3. TEM observations

Fig. 7 shows TEM micrographs of the microstructure of the original specimen and the subsurface layers (20–30 μm deep from the top surface) of the specimens that underwent the argon-UIT and cryo-UIT processes. Compared to the original specimen contained austenite grains of a few micrometers (Fig. 7a), the UIT processed samples are characterized by the multiphase microstructures regardless the processing environment used.

In the specimen processed with argon-UIT for 50 s, typical microstructures contain twins of nanoscale thickness and sometimes the shear bands (Fig. 7b,c). The areas between the twins/bands, which are of tens/hundreds of nanometers in thickness, contain a high density of

dislocations that tend to form thick dislocation boundaries. The twins of several systems can also be observed, and the intersections of these twins/shear bands usually serve as nuclei of α'-martensite. An appropriate SAED pattern clearly shows the existence of several phases and twins (inset in Fig. 7b,c). The dark field image was obtained in the spot indicated by a white marker in the SAED pattern. When the argon-UIT process proceeds, the extremely twinned/shear banded areas coexist with the areas of the well-formed dislocation cell structure (Fig. 7d). The shear bands usually intersected many grains/subgrains simultaneously, while the dislocation cell structure was formed in the grains, which were positioned outside these shear bands. A dislocation cell structure is known to be rather unusual for low-SFE materials like the studied austenitic steel owing to a large splitting of partial dislocations in the slip plains. Nevertheless, it was already observed earlier in the laser shot peened and vacuum-UIT processed specimens of the steel AISI 321 [7] or in SMAT-ed steel AISI 304 [3]. The argon-UIT process seemingly facilitates both the hindering of the partials splitting and the promotion of the cross-slip of screw components of dislocations. These dislocation movements can be promoted by the formation of different obstacles (stacking faults, nano-scale carbides etc.) and compressive internal stresses, on the one hand, and a large number of the straining-induced vacancies, on the other hand.

Microstructures of the cryo-UIT processed specimens are more complex (Fig. 7e-g). Additionally to twins, which amounts are much higher than those in the argon-UIT processed samples, a lot of ε-martensite is found at the different stages of the cryo-UIT process (different strain extents). At the strain extent of $\bar{e} \approx 0.7$ (after cryo-UIT for 150 s), the intersections of stacking faults (ε-lamellae) leading to the nucleation of α'-martensite can be easily found (Fig. 7e). Further, the cryo-UIT process results in the formation of the microstructure, which still contains austenite twins of nano- and submicronic size, a lot of α'-martensite, and a small fraction of ε-martensite (hcp). Considering the dark field image presented in Fig. 7g, two different morphologies of α' phase can be observed. A system of parallel martensitic laths of 50–120 nm thick coexists with the submicron-sized islands of α'-martensite. The latter are probably formed owing to the fragmentation of long deformation twins. The SAED patterns registered for both cases contain diffraction spots from hcp ε-phase (insets in Fig. 7e and Fig. 7f,g) as well as the spots of twins, γ and α' phases. Thus, the multistage $\gamma \to \varepsilon \to \alpha'$ transformation is evidently involved in the deformation mechanisms at cryo-UIT. It correlates well with the data of XRD analysis (Fig. 4). Such transformation sequence is well documented for austenitic steels deformed either by tension [10,17,22] or by multiple impact loading [3,7].

Fig. 8 compares the typical microstructural features observed in the top surface layers of the specimens processed with UIT in different environments (different temperatures). Appropriate histograms analyze the size of critical structural elements affecting the strength (the hardness magnitudes) of the UIT processed specimens. The heavily twinned microstructures were observed in the argon-UIT processed specimen (Fig. 8a), and two systems of parallel twin lamellae form rectangular blocks of 200–700 nm in size (Fig. 8b). The inter-twin spacing and twin volume fraction were determined by direct TEM observations of a lot of images and compared with the literature data in Table 2. The term 'twin volume fraction' is applied here only to the outmost surface layer (~ 20 μm), which microstructure was analyzed by TEM. More accurate information regarding the probability of deformation twins can be obtained using XRD method giving more integral information in comparison with local TEM analysis [45]. Often, large areas with the well-formed dislocation cell structures can also be found throughout the top surface layer of the argon-UIT processed specimen (Fig. 8c). The average cell size ranges 100–600 nm (Fig. 8d). Conversely, the outmost surface of the cryo-UIT processed sample contains mainly nanoscale grains/twins/bands with boundaries of high misorientations (Fig. 8e). SAED pattern clearly shows azimuthally dispersed arc-like spots, which tend to form the rings. Analysis of the
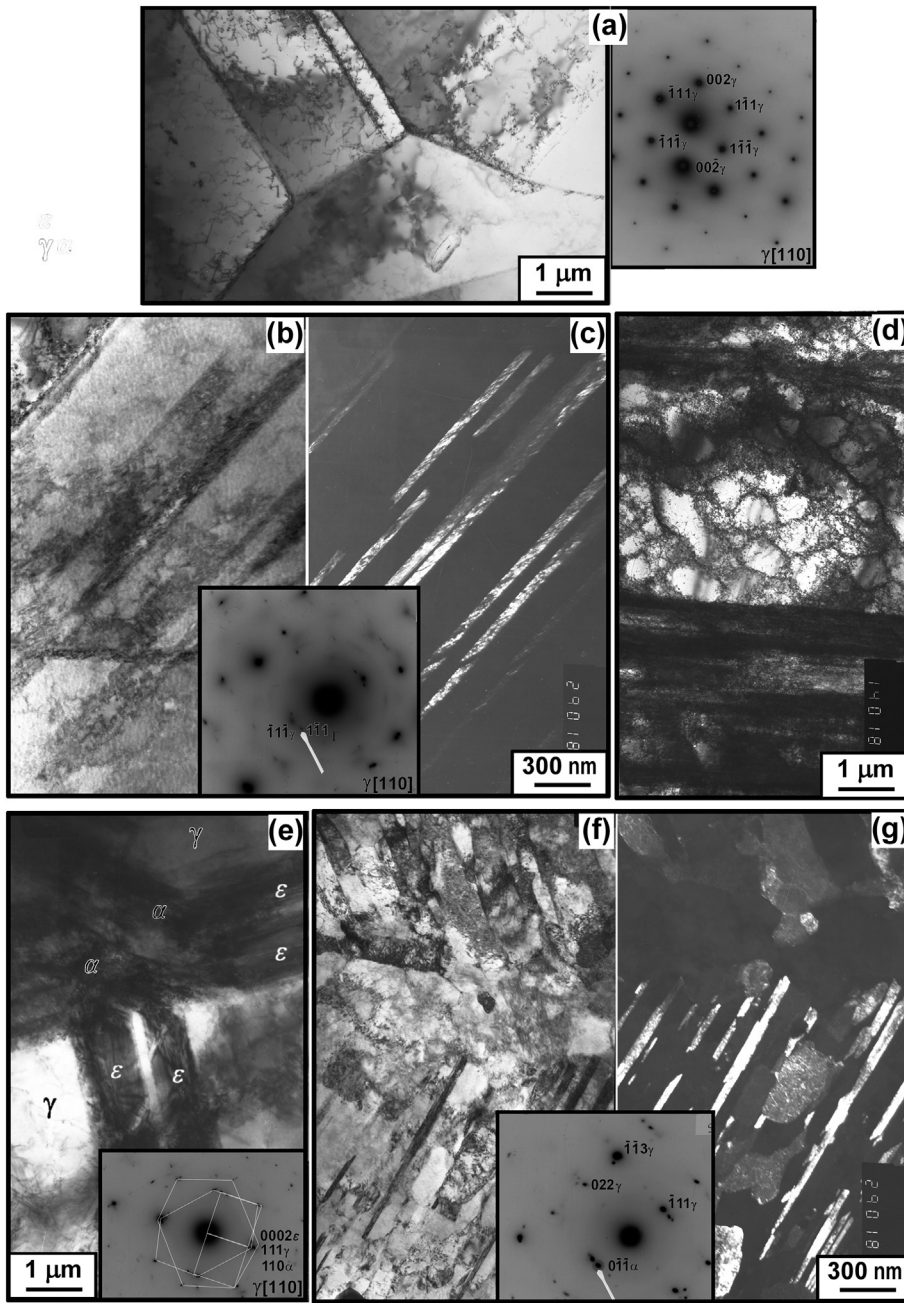
Fig. 7. Bright-field TEM image and SAED pattern of the original specimen (a), bright-field (b, d) and dark-field (c) TEM images and SAED pattern (inset in b, d) of the specimens argon-UIT processed for 50 (b, c) and 150 s (d), and bright-field (e, f) and dark-field (g) TEM images and with SAED patterns of the specimens cryo-UIT processed for 150 (e, f) and 200 s (g).

diameters of these rings and proper lattice parameters ($a_\gamma = 0.3575$ nm, $a_{\alpha'} = 0.2868$ nm), the presence of both the γ and α' phases was confirmed. A lot of dislocations associated with the boundaries of the twin blocks are generated (Fig. 8a). Their interaction promotes forming the cell-like structures inside the twin blocks. Similarly, many dislocations are also present inside the dislocation cells and ultra-fine grains (Fig. 8c,e).

During the argon-UIT process, the high strain rate plastic deformation evidently leads both to intensive twinning and to the generation of dislocation lines, tangles and walls in the original coarse grains and inside the twin blocks. Further straining accompanied with relatively high transient temperature rise may results in the rearrangement of these dislocation tangles/walls into subgrain boundaries. The latter could finally evolve into nanoscale grains through dynamic recrystallization [8,11]. In the case of cryo-UIT, the twinning and shear banding are more effective and the dynamic recrystallization is hindered. Thus, a microstructure with finer grains is formed.

4. Discussion

4.1. Microstructure – hardening relationship

Taking into consideration the microstructural features revealed by XRD analysis (Section 3.2) and TEM observations (Section 3.3) various hardening mechanisms can be suggested to give a more precise explanation of the hardness behavior (Fig. 2a, Fig. 3d) and to compose some kind of a general expression describing the hardening process. First of all, the surface layer of the deformed stainless steel becomes a composite-like material, i.e. it comprises the α'-martensite 'reinforcing' more ductile austenite 'matrix'. Then, the so-called friction stress σ_0, which naturally would be different for the fcc γ-austenite and bcc (bct) α'-martensite phases [46]. Additionally, both of the main phases (γ and α') were proved to be highly dislocated (Fig. 6c, Fig. 7, Fig. 8). Thus, Taylor's term of hardening should be included in a general hardening law. In the well-known expression based on the reciprocal square root
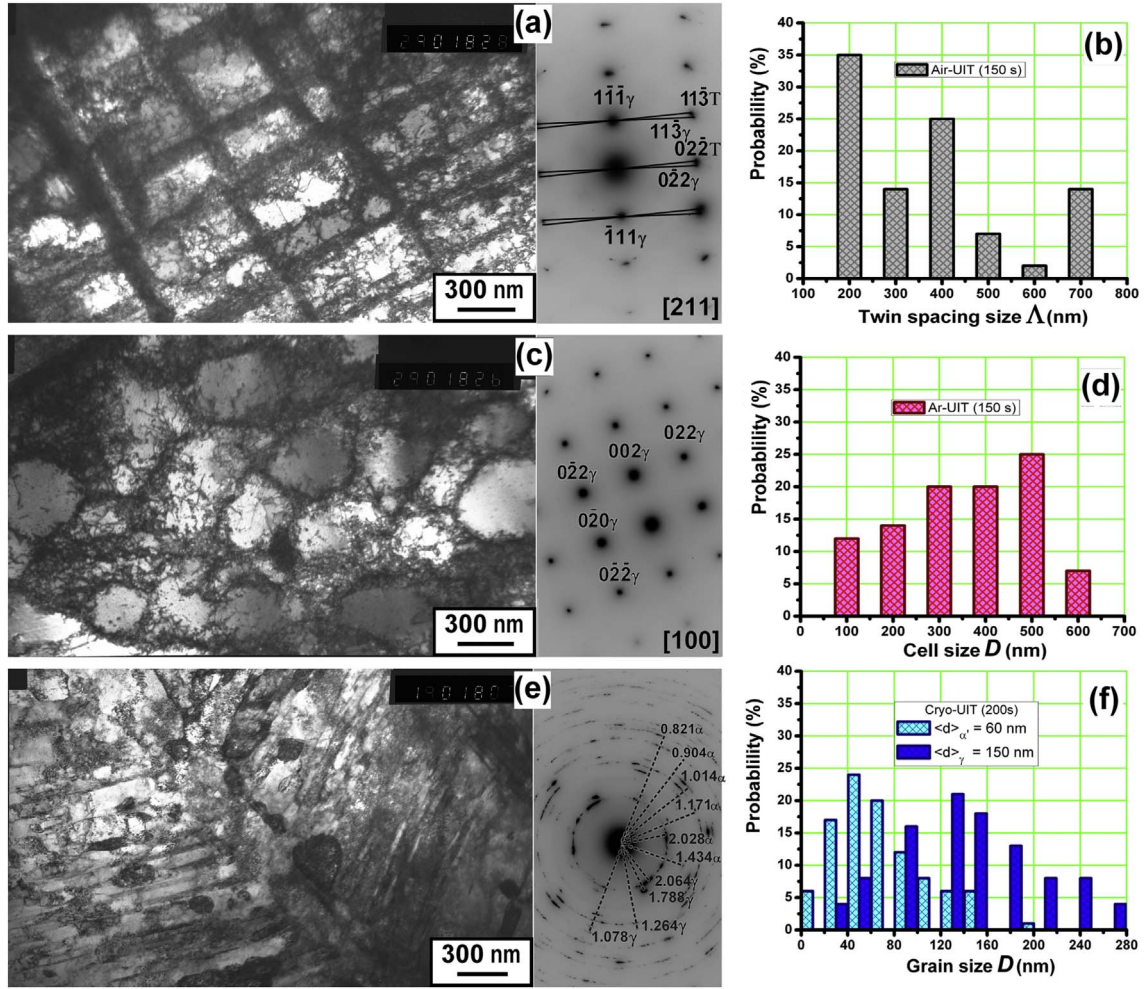
Fig. 8. Bright-field TEM images of microstructure with SAED patterns (a, c, e) supplemented with histograms of the size distributions of twin spacings (b), cells (f), and grains (f) in the top surface layers of the specimens argon-UIT processed for 150 s (a–d) and cryo-UIT processed for 200 s (e, f).

of dislocation density ρ, other parameters (constant $\alpha \approx 0.2$–1, Taylor constant M (≈ 3.06 for fcc austenite and ≈ 2 for bct martensite), shear modulus $G \approx 84$ GPa, and Burgers' vector $b \approx 0.25$ nm) should be chosen accordingly for γ and α′ phases [46]:

$$\Delta\sigma = \alpha M G b \rho^{-1/2}. \tag{10}$$

Further, a couple of terms of the Hall-Petch type should be taken into account. Firstly, this well-known law of the reciprocal square root of the grain size D_g should be applied to describe the ultrafine grains formed after the cryogenic UIT process (Fig. 7f,g, Fig. 8e,f):

$$\Delta\sigma = \sigma_0 + K_1 D_g^{-1/2}. \tag{11}$$

Additionally, following the work [47] describing the contribution of deformation twins to yield stress in the shock-loaded stainless steel 304, and assuming that the twin boundaries strengthen the material identically to the grain boundaries, the reciprocal square root of the grain size D_g should be supplemented with a similar term corresponding to the inter-twin spacings [47]:

$$\Delta\sigma = K_2 \Lambda^{-1/2} \tag{12}$$

However, it was shown recently for nanotwinned nickel alloy [47] that the $\Lambda^{-1/2}$ dependence for the twin boundaries is valid only when the twin spacing is large ($\Lambda > 150$ nm), but for the small twin spacing ($\Lambda < 100$ nm) the Λ^{-1} dependence of the hardness is conversely valid:

$$\Delta\sigma = K_2 \Lambda^{-1} \tag{13}$$

It was explained by the change of the hardening mechanism from

the mechanism consisting in the interactions of twin boundaries with dislocations to that dictated by the spreading ability of the dislocations inside the twins/twin spacings [48]. Assuming these conclusions to be valid in our case, and considering the microstructure observed by TEM in the surface layer of the argon-UIT processed specimen (Fig. 7b,d, Fig. 8a,b, Table 2), the $\Lambda^{-1/2}$ dependence for the twin boundaries hardening (Eq. (12)) can be adopted for the argon-UIT processed surface layer. Conversely, the cryo-UIT processed specimen contained numerous nanotwins would be better described using the Λ^{-1} dependence (Eq. (13)).

Besides, the dislocation cells (Fig. 7d, Fig. 8c) are also effective hardening factor, which should be taken into account for the argon-UIT processed specimens by applying the term with the reciprocal cell size D_c [45]:

$$\Delta\sigma = K_3 D_c^{-1} \tag{14}$$

To account for the hardening caused by the dislocation tangled inside the cells or twin blocks, the Taylor's term described earlier by Eq. (10) should be used. Then, using the appropriate material's constants and the well-known Tabor's relation connecting the yield stress and hardness of material ($H \approx 3\sigma_Y$), a general expression describing hardness can be written by aggregation of the appropriate terms from the above-described list.

Using the above-described expressions and experimentally assessed magnitudes of dislocation density ρ and grain/cell/twin spacing size a total hardening can be estimated. For this purposes the magnitude of friction stress σ_0 (Peierls-Nabarro stress $\sigma_{P\text{-}N} \approx 60$ MPa for fcc austenite
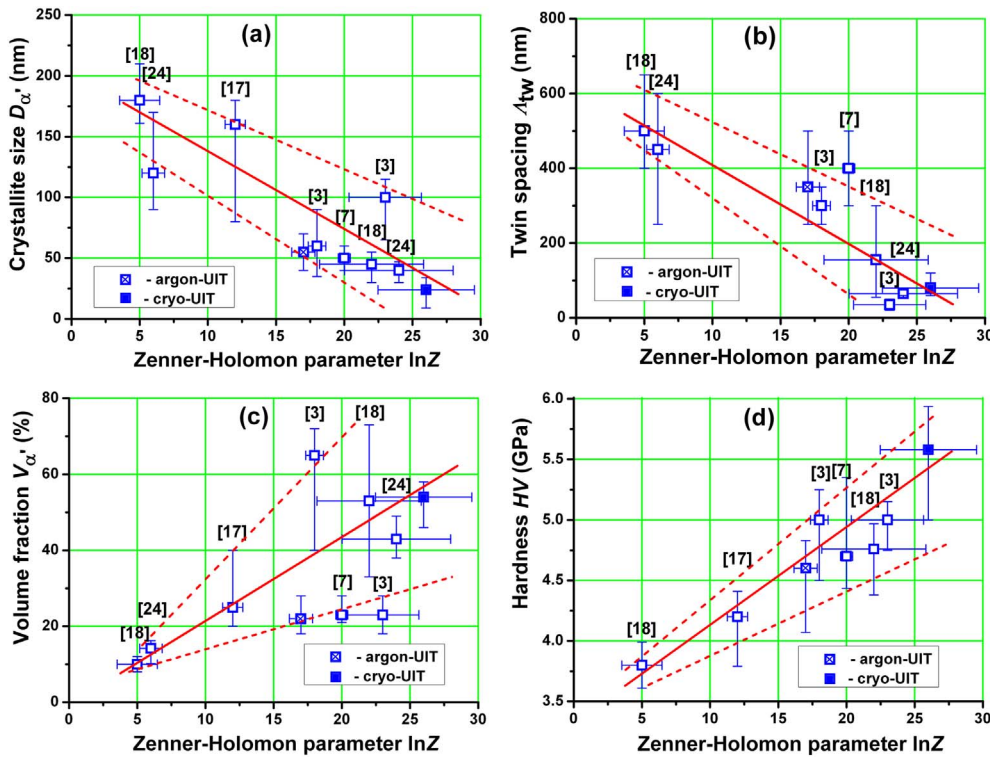
Fig. 9. Plots of the crystallite size $D_{\alpha'}$ (a), twin spacing Λ_{tw} (b), the volume fraction of α'-martensite $V_{\alpha'}$ (c), and surface microhardness HV (d) on Zener-Hollomon parameter lnZ. Data for the argon-UIT and cryo-UIT processes are respectively indicated with the crossed and solid squares.

and ≈ 30 MPa for bcc phase) and values of $K_1 \approx 0.38$ MPa m$^{1/2}$ for austenite, $K_1 \approx 0.7$ MPa m$^{1/2}$ for bcc phase, $K_2 \approx 0.6$ MPa m$^{1/2}$, and $K_3 \approx 0.12$ MPa m$^{1/2}$ coefficients were applied [46,48,49]. Rough estimations of Taylor's term of hardening (Eq. (10)) on the base of dislocation densities shown in Fig. 6c gives $\Delta\sigma_\rho = 130...270$ MPa, whereas the Hall-Petch terms (Eqs. (11)–(14)) range from 960 to 2700 MPa. As a result, the total values of $\Delta\sigma$ ($H \approx 3\Delta\sigma$) estimated for the argon-UIT and cryo-UIT processed specimens were ~ 1.09 GPa (3.27 GPa) and 2.97 GPa (8.9 GPa), respectively. Comparison of theses estimated values with the experimentally measured microhardness show that for the case of the argon-UIT processed specimen H is close but slightly underrated than the experimental HV on the specimen surface (curve 1 in Fig. 3d). The estimated hardness of the cryo-UIT processed specimen is closer to the measured surface microhardness after cryo-UIT for 250 s (curve 4 in Fig. 3d) but is much higher than that after cryo-UIT for 150 s (curve 3 in Fig. 3d). These discrepancies can be explained by some inhomogeneity of the microstructure and by the uncertainty of the power of different hardening mechanisms and the method of their additivity. A summation can be performed either using a 'stress additivity' principle (both the week and strong obstacles are overcome simultaneously) or the 'stress squares' principle, when the overcoming process is sequential [50].

4.2. Processing parameters – hardening relation

The above-considered microscopic mechanisms, which are responsible for the hardening of the surface layers severely deformed during the UIT process, are in intimate correlation with the intrinsic parameters (SFE) affecting the microstructure and phase transformations in the stainless steel AISI 321 (see Sections 3.2 and 3.3). At the same time, this consideration would remain insufficient without the understanding of the effects of the UIT processing parameters. Thus, it is of interest to analyze the influence of the extrinsic parameters, such as strain rate and processing temperature, which are combined in Zener-Hollomon parameter Z (Eq. (2)).

The main microstructural characteristics observed in this study are compared to the appropriate data reported for different austenitic steels

underwent severe plastic deformation at room and cryogenic temperatures by applying various methods (Table 2). The majority of these data were collected for similar strain extents ($\bar{e} \approx 1.0$) (except for the SMAT [3], which was analyzed at $\bar{e} = 0.07$–0.2). For better clarification, Fig. 9 shows the plots of the grain/crystallite size, twin spacing, the volume fraction of α'-martensite, and surface hardness in relation with the lnZ parameter.

It is seen that the analyzed literature data can be well described by the linear functions despite a large scattering of the data. Both the grain/crystallite size (Fig. 9a) and twin spacing (Fig. 9b) naturally decrease with Z value. On the contrary, the $V_{\alpha'}$ generally increases with Z value tough this dependence is characterized with the highest scattering of the data (Fig. 9c). It can be explained by a concurrent influence of the strain rate and the temperature decrease. Conversely to the effect of the cryogenic temperature, which undoubtedly increases the $V_{\alpha'}$, the influence of the strain rate is not so unambiguous. It was earnestly shown that the strain rate during SMAT-L and SMAT-H processes plays a key role in the intensity of martensitic transformation as well as of twinning/shear banding [3]. The stain rate higher than 10^4–10^5 may hinder α'-martensite formation [3]. Moreover, the adiabatic heating and transient temperature rise on the deformed surface layers can indirectly promote the reverse $\alpha' \rightarrow \gamma$ transformation [42,43] leading to the decrease of $V_{\alpha'}$, and as a result, to a possible diminution in the final hardness. Nevertheless, the ascending dependence of the surface hardness with Z value is observed (Fig. 9d).

5. Summarizing remarks

Ultrasonic impact treatment (UIT) of stainless steel AISI 321 was carried out at in the argon environment (room temperature) and in the liquid nitrogen (at cryogenic temperature) in constrained conditions with application of the same mechanical energy applied to the specimens.

The time dependencies of the surface hardness after the cryo-UIT and argon-UIT processes were observed to be of sigmoidal and parabolic shapes, respectively. This finding correlates well with the literature data of cryogenic tensile behavior of stainless steels, and it was

explained by the difference in the intensity and sequence of phase transformations. Both the maximum *HV* magnitude and the thickness δ*h* of the hardened layers were larger for the cryo-UIT processed specimens. The thickness δ*h* increased at more prolonged processing time and decreases at lower processing temperatures.

As shown by XRD, OM, TEM and SAED analyses, the microstructural evolution in the surface layers of the deformed specimens was responsible for the observed *HV* behavior. The volume fractions of the deformation-induced α′-martensite were estimated using XRD approach and by magnetic and density measurements. Compared to argon-UIT, the cryo-UIT process generated a higher density of deformation twins and stacking faults. In addition, a higher volume fraction of α′-martensite (~53%) and retained ε-martensite (~3.5%) were observed after cryo-UIT in the deeper surface layers (~200 μm).

The argon-UIT process led to the formation of either rectangular twin blocks or dislocation cells, which size ranged 200–500 nm. Conversely, after cryo-UIT ($\bar{e} \approx 0.95$), a nanoscale grain structure of heterogeneous nature (α′ and γ phases) formed in the outmost surface layer simultaneously with the areas filled with networks of deformation twins and stacking faults. The minimum grain size of α′-martensite $D_{\alpha'}$ and austenite D_{γ} was respectively 25 and 45 nm, and twin thickness/spacing was of 60–120 nm in this case. Both types of microstructure contributed to the material strength and resulted in the higher hardness of the cryo-UIT processed specimens (~5–5.66 GPa) in comparison with that of the argon-UIT processed ones (~4.3 GPa).

Accounting for the literature value of the activation energy for deformation of the stainless steel ($Q = 33.4$ kJ/mol), the magnitudes of the Zener-Hollomon parameter ln*Z* for the argon-UIT and cryo-UIT processes were respectively estimated to be 17 and 26. The observed microstructural features (grain size, twin thickness/spacing, the volume fraction of α′-martensite) and the surface hardness *HV* were successfully incorporated into the linear dependencies of these parameters collected from the literature data for various treatments performed at different strain rates and temperatures (the ln*Z* are within the interval 5–26).

Acknowledgement

References

[1] T. Wang, J. Yu, B. Dong, Surface nanocrystallization induced by shot peening and its effect on corrosion resistance of 1Cr18Ni9Ti stainless steel, Surf. Coat. Technol. 200 (2006) 4777–4781.

[2] H.W. Zhang, Z.K. Hei, G. Liu, J. Lu, K. Lu, Formation of nanostructured surface layer on AISI 304 stainless steel by means of surface mechanical attrition treatment, Acta Mater. 51 (2003) 1871–1881.

[3] A.Y. Chen, H.H. Ruan, J. Wang, H.L. Chan, Q. Wang, Q. Li, J. Lu, The influence of strain rate on the microstructure transition of 304 stainless steel, Acta Mater. 59 (2011) 3697–3709.

[4] A.M. Gatey, S.S. Hosmani, R.P. Singh, Surface mechanical attrition treated AISI 304L steel: role of process parameters, Surf. Eng. 32 (2016) 69–78.

[5] G. Manimaran, M. Pradeep Kumar, R. Venkatasamy, Influence of cryogenic cooling on surface grinding of stainless steel 316, Cryogenics 59 (2014) 76–83.

[6] B.N. Mordyuk, G.I. Prokopenko, M.A. Vasylyev, M.O. Iefimov, Effect of structure evolution induced by ultrasonic peening on the corrosion behavior of AISI-321 stainless steel, Mater. Sci. Eng. A 458 (2007) 253–261.

[7] B.N. Mordyuk, Yu.V. Milman, M.O. Iefimov, G.I. Prokopenko, V.V. Silberschmidt, M.I. Danylenko, A.V. Kotko, Characterization of ultrasonically peened and laser-shock peened surface layers of AISI 321 stainless steel, Surf. Coat. Technol. 202 (2008) 4875–4883.

[8] B.N. Mordyuk, G.I. Prokopenko, Ultrasonic impact treatment – an effective method for nanostructuring the surface layers of metallic materials, in: M. Aliofkhazraei (Ed.), Handbook of Mechanical Nanostructuring, Wiley-VCH, 2015, pp. 417–434, , http://dx.doi.org/10.1002/9783527674947.ch17.

[9] E. El-Danaf, S.R. Kalidindi, R.D. Doherty, Influence of grain size and stacking-fault energy on deformation twinning in fcc metals, Metall. Mater. Trans. A 30 (1999) 1223–1233.

[10] J. Talonen, H. Hänninen, Formation of shear bands and strain-induced martensite during plastic deformation of metastable austenitic stainless steels, Acta Mater. 55

[11] Y.S. Li, Y. Zhang, N.R. Tao, K. Lu, Effect of the Zener–Hollomon parameter on the microstructures and mechanical properties of Cu subjected to plastic deformation, Acta Mater. 57 (2009) 761–772.

[12] P. Zhang, X.H. An, Z.J. Zhang, S.D. Wu, S.X. Li, Z.F. Zhang, R.B. Figueiredo, N. Gao, T.G. Langdon, Optimizing strength and ductility of Cu–Zn alloys through severe plastic deformation, Scr. Mater. 67 (2012) 871–874.

[13] K. Huang, R.E. Logé, A review of dynamic recrystallization phenomena in metallic materials, Mater. Des. 111 (2016) 548–574.

[14] F.K. Yan, G.Z. Liu, N.R. Tao, K. Lu, Strength and ductility of 316L austenitic stainless steel strengthened by nano-scale twin bundles, Acta Mater. 60 (2012) 1059–1071.

[15] P.L. Mangonon, G. Thomas, The martensite phases in 304 stainless steel, Metal. Trans. 1 (1970) 1577–1586.

[16] C. Garion, B. Skoczeń, S. Sgobba, Constitutive modelling and identification of parameters of the plastic strain-induced martensitic transformation in 316L stainless steel at cryogenic temperatures, Int. J. Plast. 22 (2006) 1234–1264.

[17] A.K. De, J.G. Speer, D.K. Matlock, D.C. Murdock, M.C. Mataya, R.J. Comstock, Deformation-induced transformation and strain hardening in type 304 austenitic stainless steel, Metall. Mater. Trans. A 37 (2006) 1875–1886.

[18] Y. Nakao, H. Miura, Nano-grain evolution in austenitic stainless steel during multi-directional forging, Mater. Sci. Eng. A 528 (2011) 1310–1317.

[19] Y. Huang, P.B. Prangnell, The effect of cryogenic temperature and change in deformation mode on the limiting grain size in a severely deformed dilute aluminium alloy, Acta Mater. 56 (2008) 1619–1632.

[20] Z. Pu, S. Yang, G.-L. Song, O.W. Dillon, I.S. Jawahir, Ultrafine-grained surface layer on Mg–Al–Zn alloy produced by cryogenic burnishing for enhanced corrosion resistance, Scr. Mater. 65 (2011) 520–523.

[21] V. Seetharaman, R. Krishnan, Influence of the martensitic transformation on the deformation behaviour of an AISI 316 stainless steel at low temperatures, J. Mater. Sci. 16 (1981) 523–530.

[22] A.K. De, D.C. Murdock, M.C. Mataya, J.G. Speer, D.K. Matlock, Quantitative measurement of deformation-induced martensite in 304 stainless steel by X-ray diffraction, Scr. Mater. 50 (2004) 1445–1449.

[23] W.S. Park, S.W. Yoo, M.H. Kim, J.M. Lee, Strain-rate effects on the mechanical behavior of the AISI 300 series of austenitic stainless steel under cryogenic environments, Mater. Des. 31 (2010) 3630–3640.

[24] T.S. Wang, J.G. Peng, Y.W. Gao, F.C. Zhang, T.F. Jing, Microstructure of 1Cr18Ni9Ti stainless steel by cryogenic compression deformation and annealing, Mater. Sci. Eng. A 407 (2005) 84–88.

[25] J. Shi, L. Hou, J. Zuo, L. Zhuang, J. Zhang, Effect of cryogenic rolling and annealing on the microstructure evolution and mechanical properties of 304 stainless steel, Int. J. Miner. Metall. Mater. 24 (2017) 638.

[26] T. Balusamy, T.S.N. Sankara Narayanan, K. Ravichandran, I.S. Park, M.H. Lee, Influence of surface mechanical attrition treatment (SMAT) on the corrosion behaviour of aisi 304 stainless steel, Corros. Sci. 74 (2013) 332–344.

[27] C. Ye, S. Suslov, D. Lin, G.J. Cheng, Deformation-induced martensite and nanotwins by cryogenic laser shock peening of AISI 304 stainless steel and the effects on mechanical properties, Philos. Mag. 92 (2012) 1369–1389.

[28] C. Ye, A. Telang, A.S. Gill, S. Suslov, Y. Idell, K. Zweiacker, J.M.K. Wiezorek, Z. Zhou, D. Qian, S.R. Mannava, V.K. Vasudevan, Nano-crystal surface modification in 304 austenitic stainless steel for high strength and high ductility, Mater. Sci. Eng. A 613 (2014) 274–288.

[29] T. Iwamoto, Multiscale computational simulation of deformation behavior of trip steel with growth of martensitic particles in unit cell by asymptotic homogenization method, Int. J. Plast. 20 (2004) 841–869.

[30] B.N. Mordyuk, O.P. Karasevskaya, G.I. Prokopenko, N.I. Khripta, Ultrafine-grained textured surface layer on Zr-1%Nb alloy produced by ultrasonic impact treatment for enhanced corrosion resistance, Surf. Coat. Technol. 210 (2012) 54–61.

[31] M.A. Vasylyev, S.P. Chenakin, L.F. Yatsenko, Nitridation of Ti-6Al-4V alloy under ultrasonic impact treatment in liquid nitrogen, Acta Mater. 60 (2012) 6223–6233.

[32] M.A. Vasylyev, S.P. Chenakin, L.F. Yatsenko, Ultrasonic impact treatment induced oxidation of Ti-6Al-4V alloy, Acta Mater. 103 (2016) 761–774.

[33] M.A. Vasylyev, B.N. Mordyuk, S.I. Sidorenko, S.M. Voloshko, A.P. Burmak, Peculiarities of structure and phase formations in the surface layers of 2024 alloy at UIT in various environments, Metallofiz. Noveishie Tekhnol. 39 (2017) 49–68 in Ukrainian 10.15407/mfint.39.01.0049.

[34] M.A. Vasylyev, B.N. Mordyuk, S.I. Sidorenko, S.M. Voloshko, A.P. Burmak, Corrosion of 2024 alloy after ultrasonic impact cladding with iron, Surf. Eng. (2017), http://dx.doi.org/10.1080/02670844.2017.1334377.

[35] H. Huang, J. Ding, P.G. McCormick, Microstructural evolution of 304 stainless steel during mechanical milling, Mater. Sci. Eng. A 216 (1996) 178–184.

[36] W.-S. Lee, T.-H. Chen, C.-F. Lin, Z.-Y. Li, Effects of strain rate and temperature on shear properties and fracture characteristics of 316L stainless steel, Mater. Trans. 53 (3) (2012) 469–476.

[37] C. Suryanarayana, Mechanical alloying and milling, Progress in, Mater. Sci. 46 (2001) 1–184.

[38] E.G. Astafurova, G.G. Maier, E.V. Naydenkin, G.I. Raab, P.D. Odessky, S.V. Dobatkin, The influence of initial state of low-carbon steels on structure and mechanical properties under equal-channel angular pressing, Mathematics and Mechanics Physics, 324(2) Bulletin of the Tomsk Polytechnic University, 2014, pp. 107–117 http://www.lib.tpu.ru/fulltext/v/Bulletin_TPU/2014/v324/i2/18.pdf in Russian.

[39] J. Talonen, P. Aspegren, H. Häninnen, Comparison of different methods for measuring strain induced a′-martensite content in austenitic steels, Mater. Sci. Technol. 20 (2004) 1506–1512.

[40] K.P. Staudhammer, L.E. Murr, S.S. Hecker, Nucleation and evolution of strain-in-duced martensitic (b.c.c.) embryos and substructure in stainless steel: a transmis-sion electron microscope study, Acta Metall. 31 (1983) 267–274.

[41] Z. Ni, X. Wang, J. Wang, E. Wu, Characterization of the phase transformation in a nanostructured surface layer of 304 stainless steel induced by high-energy shot peening, Phys. B Condens. Matter 334 (2003) 221–228.

[42] A.Y. Chen, J.B. Zhang, H.W. Song, J. Lu, Thermal-induced inverse γ/α' transfor-mation in surface nanocrystallization layer of 304 stainless steel, Surf. Coat. Technol. 201 (2007) 7462–7466.

[43] H. Sato, A. Namba, M. Okada, Y. Watanabe, Temperature dependence of reverse transformation induced by shot-peening for SUS 304 austenitic stainless steel, Materials Today: Proceedings 2S (2015) S707–S710.

[44] S. Curtze, V.-T. Kuokkala, A. Oikari, J. Talonen, H. Hänninen, Thermodynamic modeling of the stacking fault energy of austenitic steels, Acta Mater. 59 (2011) 1068–1076.

[45] A.L. Ortiz, J.-W. Tian, L.L. Shaw, P.K. Liaw, Experimental study of the microstructure and stress state of shot peened and surface mechanical attrition treated nickel alloys, Scr. Mater. 62 (2010) 129–132.

[46] V.I. Trefilov, Yu.V. Milman, S.A. Firstov, Basic physics of strength and plasticity of refractory metals, Naykova Dumka, Kiev, 1975 (in Russian).

[47] L.E. Murr, E. Moin, F. Greulich, The contribution of deformation twins to yield stress: The Hall-Petch law for inter-twin spacing, Scripta Metal. 12 (1978) 1031–1035.

[48] L.L. Shaw, A.L. Ortiz, J.C. Villegas, Hall–Petch relationship in a nanotwinned nickel alloy, Scr. Mater. 58 (2008) 951–954.

[49] S.B. Nizhnik, E.A. Dmitrieva, Studies on strain-hardening models for structural steels at a directed reduction in sizes of their structural elements, Strength Mater. 43 (4) (2011) 464–470.

[50] N. Tsuchida, Y. Tomota, H. Moriya, O. Umezawa, K. Nagai, Application of the Kocks–Mecking model to tensile deformation of an austenitic 25Cr–19Ni steel, Acta Mater. 49 (2001) 3029–3038.